

Hybrid Convolutional Neural Network Architecture for Defect Detection in Photovoltaic Cells

Alan Marques da Rocha
Federal University of Ceará (UFC)
Technology Center
Fortaleza, CE, Brazil

Francilândio Lima Serafim
Graduate Program in Electrical and Computer Engineering,
Federal University of Ceará, campus Sobral (UFC)

Antonia Alana Claudino Sousa
Federal Institute of Education,
Science and Technology of Ceará (IFCE)
Sobral, CE, Brazil

Wendley Souza da Silva
Graduate Program in Electrical and Computer Engineering,
Federal University of Ceará, campus Sobral (UFC)

ABSTRACT

The expansion of installed capacity in photovoltaic (PV) generation systems requires automated methods for detecting faults in their constituent cells. This paper proposes a hybrid convolutional neural network (HCNN) model for fault detection in electroluminescence (EL) images of PV panels. The model utilizes the ResNet50 and VGG16 topologies for feature extraction and the support vector machine (SVM) for detecting defective cells. Fine-tuning the model's hyperparameters through a genetic algorithm resulted in accuracies of 98.17% and 99.67% in classification experiments conducted with two public datasets. The challenges posed by the heterogeneity of these datasets in model training were addressed through data augmentation techniques and contrast enhancement. The results highlight the effectiveness of the HCNN, demonstrating its potential as a robust solution for the automated detection of defects in PV cells, which is essential for maintaining optimal energy conversion efficiency and extending the operational lifespan of these systems.

General Terms

Computer Vision, Deep Learning, Genetic Algorithms, Photovoltaic Systems

Keywords

Electroluminescence, HCNN, Evolutionary genetic algorithms, Fault detection

1. INTRODUCTION

The demand for clean and renewable energy has led to the large-scale installation of photovoltaic (PV) solar power plants worldwide. Additionally, the reduction in the cost of photovoltaic components has encouraged the widespread implementation of small-scale generation units.

However, PV generation has its own limitations. Improper maintenance of PV cells can result in failures that compromise the efficiency and longevity of these systems. Therefore, early fault detection and preventive correction can prevent significant economic and environmental losses.

Defects in PV cells can arise during manufacturing, transportation, and operation. Failures may result from electrical issues such as disconnections, open circuits, and short circuits in PV modules [5]. Overheating due to these conditions appears in PV cells as hotspots, leading to energy loss and reduced power output [23]. Furthermore, these problems pose risks to both humans and the environment, highlighting the importance of early identification and resolution of faults in these systems.

Environmental factors also play a crucial role in PV system failures and energy losses. Storms, hail, partial shading from trees, dust, and bird droppings can cause defects in PV cells, such as corrosion, hotspots, cracks, microcracks, moisture ingress, fractures, and delaminations [6].

Infrared thermography and electroluminescence (EL) imaging [20] are commonly used methods for diagnosing the integrity of PV cells based on images. Due to its inherent practicality and accuracy, infrared thermography has been widely researched [6, 3], as the operating temperature of the modules is an important parameter for hotspot detection. EL imaging [18, 26] is based on the principles of charge carrier recombination and photon emission when an electric voltage is applied to a PV cell. The excess energy released as photons generates images from the emission of visible and infrared light [28], revealing spatial variations in light-to-electricity conversion efficiency and providing valuable information about the quality and uniformity of solar cells.

Machine learning (ML) algorithms based on images [2] and voltage/current characteristics have received attention for fault detection in PV modules [30, 19, 27, 15]. Image processing-based methods extensively adopt ML to distinguish between functional and non-functional PV systems [24].

This article presents a method for the automatic recognition of defective monocrystalline silicon (Si-m) and polycrystalline silicon (Si-p) PV cells through their EL images. The proposed method uses a hybrid convolutional neural network (HCNN), composed of a convolutional neural network (CNN) for image feature extraction and a support vector machine (SVM) to classify cells as functional or non-functional. The proposed network was trained and classified using a dataset widely used in the literature with data augmentation (DA) techniques to expand the number of training samples. Moreover, the method includes a preprocessing (PP) step for the images and genetic algorithms (GA) for fine-tuning the CNN hyperparameters. This article contributes with a method for hyperparameter selection that enables fast convergence, overfitting control, and optimal generalization ability, in addition to a CNN architecture that is competitive in both performance and complexity.

The remainder of this article is organized as follows: Section 2 provides a comprehensive overview of works that use ML algorithms for fault detection in PV cells. Section 3 describes the proposed HCNN model, the dataset used for its validation, the hyperparameter tuning process, and the training methodologies. Section 4 discusses the evaluation metrics used for the proposed models. Section 5 presents and discusses the results obtained and provides an analysis of the validation metrics used to evaluate the model's performance. Finally, Section 6 summarizes the main conclusions of this work and suggests possible directions for future research.

2. RELATED WORKS

The following section reviews studies that use ML algorithms in image processing techniques to identify and classify faults in PV modules.

[15] combined CNN and SVM to classify defects in monocrystalline (Si-m) and polycrystalline (Si-p) PV cells using datasets D1 (2,624 images, two classes) and D2 (1,028 images, three classes). Feature extraction was performed using VGG16, and classification with SVM achieved accuracies of 99.49% (D1) and 99.46% (D2). No preprocessing techniques or hyperparameter tuning were applied.

[16] proposed a model based on ResNet to detect microcracks in Si-p cells from EL images. The method included feature fusion, transfer learning, and DA using mirroring and Fourier filtering to reduce noise. The local binary pattern was used to highlight linear microcracks. The model achieved 99.11% accuracy.

[29] developed a hybrid model to detect linear features in EL images of Si-p cells, with a CNN composed of five million trainable parameters. The process included feature extraction using the Hessian matrix and a multiscale line detector. The model was compared with ResNet50, InceptionV3, VGG16, NASNet-A, and PNASNet, achieving 93% accuracy without DA or fine-tuning.

[12] proposed a deep feature-based method for multiclass detection and classification of defects in Si-m and Si-p cells. Features were extracted using deep neural networks and classified using SVM, k-NN, decision tree, and Naïve Bayes. Offline DA included 90°, 180°, and 270° rotations. A feature selection technique was used to reduce dimensionality and improve classification. The hybrid L-CNN approach trained from scratch achieved the best accuracies: 90.57% and 94.52% for the 4-class and 2-class datasets, respectively.

[1] analyzed Si-m and Si-p PV cells from EL images and classified them into four categories (functional, microcracks, visible cracks, and corrosion) using a DS-CNN network [21]. Preprocessing included geometric transformation. The average accuracy was 74.75%, ranging from 52% (microcracks) to 94% (corrosion).

3. PROPOSED METHODOLOGY

3.1 Materials and data

This study uses images from the photovoltaic electroluminescence (ELPV) dataset [11, 4, 10], which consists of 2,624 EL images of PV cells, with a resolution of 300×300 pixels, extracted from 44 PV modules. Figure 1 shows images of Si-m and Si-p PV cells available in the dataset, illustrating the differences between functional and non-functional cells. The Si-m cells illustrated in Figures 1(a) and 1(b) range from a functional state to defects with cracks and microcracks. The Si-p cells shown in Figures 1(c) and 1(d) exhibit a progression of defects, including cracks, fractures, and delamination, highlighting severe material degradation.

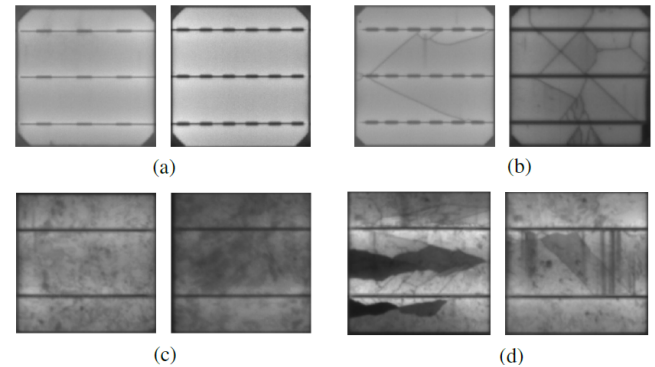


Fig. 1. EL images of silicon PV cells: (a) functional monocrystalline. (b) monocrystalline with crack and microcrack defects. (c) functional polycrystalline. (d) polycrystalline with crack, fracture, and delamination defects.

3.2 Pre-processing

The images were normalized in terms of contrast and perspective. The low contrast of EL images, due to the uneven luminescence distribution [3], limits the discrimination of subtle details, making it difficult to accurately identify defective areas.

The application of contrast limited adaptive histogram equalization (CLAHE) to the EL images involves dividing the image into small regions called tiles. In each tile, histogram equalization is performed, adjusting the distribution of gray levels and increasing local contrast in a controlled manner to avoid excessive amplification of noise. A contrast limit is set to restrict the amplification of high-contrast regions, preventing the emergence of artifacts that could obscure important information. The tile size was set to 8×8 pixels. The choice of smaller areas was made to reduce the chances of noise proliferation. However, when noise is detected, a default clipping limit factor of 2 is applied. Thus, if any histogram bin contains noise above the specified clipping factor, this noise is removed and redistributed before histogram equalization. Each tile was processed individually for histogram equalization, ensuring that the transformation was applied to all images in the augmented dataset. Figure 2(a) illustrates an example of a Si-p PV cell, while Figure 2(b) shows the result of applying the CLAHE technique during the PP step. To verify the effectiveness of the technique on the dataset, histograms of the pixel intensity of the images were generated. The analysis of the histograms in Figures 2(c) and 2(d) reveals significant changes after the application of the CLAHE technique. In the original image, the histogram shows a concentration of pixel values within a narrow range of intensities, indicating low contrast.

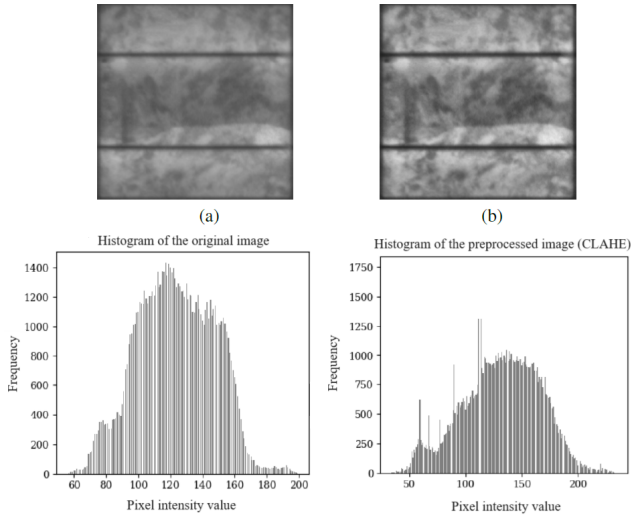


Fig. 2. (a) Original image of the Si-p PV cell. (b) Image resulting from the application of the CLAHE technique. (c) Histogram of the pixel intensity of the original image. (d) Histogram of the pixel intensity after the application of the CLAHE technique.

On the other hand, the histogram of the image processed by CLAHE exhibits a more uniform distribution of pixel intensities. This redistribution indicates a significant increase in the image contrast. With the pixel values more uniformly distributed across the entire range of intensities, previously obscured details become more visible.

This study employed four DA techniques: 1) image rotation by 90° clockwise and counterclockwise to preserve the original characteristics, 2) mirroring, 3) blurring, and 4) a 20% increase in brightness. The resulting dataset, referred to here as DS2, comprised 13,120 images of PV cells, maintaining the original proportion of functional and non-functional cells.

3.3 Hybrid convolutional neural network

The construction of the HCNN for defect classification in PV cells proposed in this work combines the robustness of CNNs in feature extraction with the precision of SVM in classification. The process involves three main steps: genetic fine-tuning (GFT), definition of the hyperparameter search space (see Table 1), and configuration of the SVM parameters. Figure 3 illustrates the architecture of the network used for feature extraction. As illustrated, only the convolutional, max-pooling, and ReLU layers were used for feature extraction, without the fully connected layers. These were replaced by the SVM for classification.

3.3.1 Genetic fine-tuning. GFT uses concepts from genetic algorithms (GA) to optimize the hyperparameters of the CNN. GAs are inspired by the process of natural evolution and use operations such as selection, crossover, and mutation to evolve solutions over several generations [14]. The hyperparameters of a CNN, such as network depth, the number of filters in each convolutional layer, filter size, learning rate, activation function type, among others, are encoded as genes in a chromosome, where each chromosome represents a unique CNN configuration.

To better understand the process of evolutionary selection in GFT, the steps proposed in the works of [33] and [32] were used, in which:

Table 1. Hyperparameter search space: types of hyperparameters, their possibilities, and quantities.

Hyperparameter Type	Possibilities
CNN	ResNet50, VGG16
Number of Layers	1, 2
Neurons in Layer 1	512, 768, 1024
Neurons in Layer 2	64, 128, 256, 512, 768, 1024
Activation Function	tanh, relu, selu, elu, exponential
Optimizer	adam, SGD, rmsprop, adadelta
Dropout	30%, 40%, 50%, 60%

- **Individual:** A pre-trained CNN with ImageNet (ResNet50 and VGG16), whose hyperparameters are contained in an attribute vector that specifies the number of layers, the number of neurons per layer, the activation function, the optimizer, etc.
- **Initial population:** An initial population of 50 individuals was created, considering that this value allows for a good initial sampling of individuals, all generated randomly and without duplicates.
- **Reproduction:** Two individuals were selected through a stochastic sampling roulette with replacement [9]. Each individual is chosen based on their fitness to solve the problem.
- **New individual:** In each reproduction, a new individual is generated, inheriting characteristics from both the father and the mother in a process called crossover.
- **Mutation:** Whenever a new individual is generated by crossover, mutation can alter a genotype in its attribute vector (a hyperparameter). The probability of mutation in this work is 7%, a value that is not so high as to prevent the transmission of parental characteristics, nor so low as to prevent the emergence of new characteristics.
- **Selection of individuals for the new generation:** At the end of each generation, 60% of the individuals with the best Kappa (κ) [7] are selected, and the others are discarded. This selection allows for finding the best characteristics to solve the problem. The selected individuals will have another chance to reproduce and transmit their characteristics to future generations.
- **Stopping condition:** To avoid infinite loops, three stopping conditions were established: 1) if any individual reaches 100% κ , the algorithm must stop, as it would be impossible to obtain better results; 2) from the 10th generation, the average accuracy of the current generation is compared with the previous five generations. If the result is lower, the algorithm must stop, allowing enough time to develop good results without interruptions and ensure progression; 3) if the 100th generation is reached, the algorithm must stop, as it is considered enough time to reach a global optimum or stagnate at a local optimum.

To optimize the defect classification process, careful planning of the hyperparameter search space was necessary. Table 1 presents the types of hyperparameters, their possible configurations, and quantities. The ResNet50 and VGG16 architectures were chosen as bases for the CNNs. Both are well-established networks, recognized for their high performance in image classification tasks, and were pre-trained on the ImageNet dataset [13]. The choice of these architectures offers a balance between depth and structural simplicity, facilitating adaptation to new classification tasks.

3.3.2 Feature extraction using the CNN. After obtaining the network hyperparameters through GFT, the pre-trained ResNet50 and VGG16 networks were applied to the EL images of the PV cells,

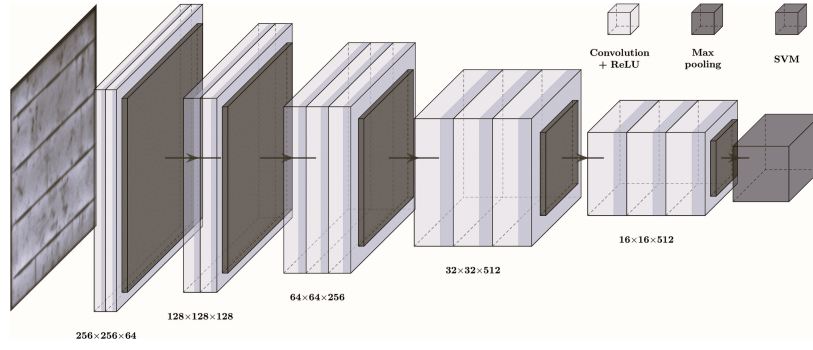


Fig. 3. Architecture of the CNN used for feature extraction.

where each convolutional layer extracted different levels of features, from simple edges to more abstract patterns, specific for defect detection in PV cells. The advantage of using pre-trained networks lies in their ability to reuse knowledge acquired in previous tasks, which accelerates the training process and improves the accuracy of feature extraction.

3.3.3 Support vector machine. The SVM [8] is a supervised learning algorithm widely used in classification tasks. It is known for its ability to handle high-dimensional data, its robustness against overfitting, particularly in scenarios with a high ratio between dimensionality and sample size, and its versatility through the use of different kernel functions, allowing the SVM to operate in the original feature space while implicitly computing scalar products in the higher-dimensional space. These characteristics allowed us to integrate the SVM as a suitable classifier in the proposed model, mainly due to its ability to manage the high-dimensional features generated by the CNNs.

The SVM parameters C and γ were determined through a grid search using the GridSearchCV class from the Scikit-Learn library [31], which explores different combinations of values for C and γ to identify the configuration that maximizes classification accuracy.

4. VALIDATION METRICS

The implementation of classification algorithms in ML requires an adequate evaluation mechanism. To ensure accuracy in performance analysis, the careful selection of training and test samples is essential.

Model evaluation was performed using k-fold cross-validation [22] with $k = 5$, an approach that improves the robustness of results by minimizing variations in training and test data. In the binary classification problem addressed, the possible outcomes are: true positive (TP) and true negative (TN) for correct classifications; false positive (FP) and false negative (FN) for model errors.

The κ index was used because it evaluates the agreement between classification methods, considering chance agreement [7, 17]. Its equation is represented by:

$$\kappa = \frac{P_o - P_e}{1 - P_e}, \quad (1)$$

where P_o is the observed agreement and P_e is the expected chance agreement, calculated by:

$$P_o = \frac{TP + TN}{TP + TN + FP + FN}, \quad (2)$$

Table 2. Agreement levels of the κ index.

Value of κ	Level of Agreement	Percentage of Reliable Data
0–0.20	None	0–4%
0.21–0.39	Minimal	4–15%
0.40–0.59	Weak	15–35%
0.60–0.79	Moderate	35–63%
0.80–0.90	Strong	64–81%
Above 0.90	Almost Perfect	82–100%

$$P_e = \frac{[(TP + TN)(TP + FP)] + [(TN + FN)(TN + FP)]}{(TP + TN + FP + FN)^2}. \quad (3)$$

Table 2 categorizes the values of κ , ranging from no agreement to almost perfect [25].

The performance metrics used in this work also include accuracy, recall, precision, specificity, and F-score, as per Equations (4)–(8). The F-score balances recall and precision, being useful for unbalanced datasets.

$$Accuracy = \frac{TP + TN}{TP + TN + FP + FN}. \quad (4)$$

$$Recall = \frac{TP}{TP + FN}. \quad (5)$$

$$Precision = \frac{TP}{TP + FP}. \quad (6)$$

$$Specificity = \frac{TN}{TN + FP}. \quad (7)$$

$$F-score = 2 \times \frac{Precision \times Recall}{Precision + Recall}. \quad (8)$$

5. RESULTS AND DISCUSSIONS

In this section, the results obtained using the proposed methodology for the DS2 dataset with PP through the CLAHE technique are presented and analyzed. Each individual generated by the GFT was trained for 100 epochs, using 80% of the images for training, 10% for testing, and 10% for validation.

5.1 Genetic fine-tuning with data augmentation

In this phase of the work, classification experiments were conducted using the DS2 dataset with GFT to find the optimal hyperparameters for the HCNN pre-trained with ImageNet. Table 3 presents the GFT results for the ten best HCNN models, where **Lay.** represents the number of layers, **N1** and **N2** are the number of neurons in layers 1 and 2, respectively, **Act.** represents the activation function, **Optim.** the optimizer used, and **Drop.** the dropout rate.

The best results were achieved with the VGG16+SVM topology, using a layer of 768 neurons, elu activation function, adadelat optimizer, and a dropout of 50%. This model reached a κ index of 80.17% and an average accuracy of 99.67%. These values indicate a strong agreement between the model's predictions and the TP and TN labels, as well as a high classification capability. The specificity of 98.41% and sensitivity of 97.12% further reinforce the model's effectiveness in correctly distinguishing between classes, minimizing both FPs and FNs.

Meanwhile, the ResNet50+SVM topology, with a layer of 1,024 neurons, relu activation function, adam optimizer, and a dropout of 40%, achieved an accuracy of 98.17% and a κ index of 85.26%, demonstrating competitive performance. The specificity of 97.34% and precision of 96.23% indicate that this model is highly effective in correctly identifying positive samples. Compared to the best VGG16+SVM result, ResNet50+SVM showed slightly lower robustness but remained competitive. The DA techniques employed contributed to this improvement, providing a broader and more varied training base, resulting in more robust and generalizable models.

The VGG16+SVM, with its simpler architecture, has fewer trainable hyperparameters compared to the ResNet50, which is deeper and more complex. This difference may explain the slightly superior performance of VGG16+SVM in terms of accuracy and the κ index. However, the additional complexity of ResNet50+SVM allows it to capture more detailed nuances of the data, reflected in its high specificity and precision.

In the visual validation step of the images, some EL images of PV cells were selected to evaluate the effectiveness of the proposed technique, as shown in the images in Table 4, which displays the predicted and expected results for each PV cell. As observed in the table, the VGG16+SVM topology correctly classified 5 out of 6 images of functional and non-functional cells. Image 6 shows a small delamination defect (dark tones) near the bottom right corner of the cell, which prevents its classification as a functional cell.

Table 5 presents a comparison of the results of this study with previous works from Section 2, focusing on defect detection in Si-m and Si-p cells. The compared studies used the ELPV dataset.

This work stands out for its use of advanced ML techniques, achieving the highest average accuracy (99.67%) among the compared studies. The sensitivity, precision, specificity, and F-score are superior or compatible with the best results in the literature. Furthermore, this is the only study to include the κ metric (80.17%) and to use GFT to optimize the hyperparameters of the ResNet50 and VGG16 models, reinforcing the reliability of the results.

The combination of HCNN and hyperparameter optimization proves to be a promising approach for defect detection in PV cells, outperforming traditional methods in performance and robustness.

6. CONCLUSIONS

The detection and classification of defects in PV panels have attracted the interest of many researchers in recent years. In this con-

text, a new model was proposed for the detection of functional and non-functional PV cells based on EL images. To increase the efficiency of inspection using machine learning models, a new methodology was proposed for the fine-tuning of the hyperparameters of the CNN models used, based on genetic algorithms.

The characteristics of CNNs and SVM were combined to form a new topology called HCNN. Furthermore, the CNN hyperparameters were obtained through GFT. The CNN accurately captures the features of the EL images of PV panels, while the SVM performs the classification step. The model was trained and evaluated on a dataset widely investigated in the literature, using DA and pre-processing techniques with CLAHE to improve image variations in the dataset.

Finally, the presented results show that the proposed model accurately detected images of functional and non-functional PV cells, with an average accuracy of 99.67% and a κ index of 80.17%, considered superior when compared to works investigated in the literature. However, a limitation of the proposed approach is its inability to correctly classify certain defects in PV cells, such as those located in the corners of the cells, which are considered part of the PV cells rather than defects. Consequently, proposals for future work should focus on the analysis of unrecognized defects to improve the efficiency of the approach. Additionally, datasets can be expanded to detect and classify all defects that may occur in Si-m and Si-p PV cells.

7. REFERENCES

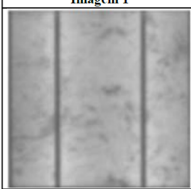
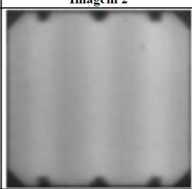


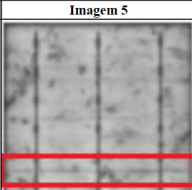

- [1] A. K. Acharya, P. K. Sahu, and S. R. Jena. Deep neural network based approach for detection of defective solar cell. *Materials Today: Proceedings*, 39:2009–2014, 2021.
- [2] M. W. Akram, G. Li, Y. Jin, X. Chen, C. Zhu, and A. Ahmad. Automatic detection of photovoltaic module defects in infrared images with isolated and develop-model transfer deep learning. *Solar Energy*, 198:175–186, 2020.
- [3] G. Balasubramani, V. Thangavelu, M. Chinnusamy, L. Mihet-Popa, U. Subramaniam, and S. Padmanaban. Infrared thermography based defects testing of solar photovoltaic panel with fuzzy rule-based evaluation. *Energies*, 13(6):1343, 2020.
- [4] C. Buerhop-Lutz, S. Deitsch, A. Maier, F. Gallwitz, S. Berger, B. Dol, J. Hauch, C. Camus, and C. J. Brabec. A benchmark for visual identification of defective solar cells in electroluminescence imagery. In *European PV Solar Energy Conference and Exhibition (EU PVSEC)*, 2018.
- [5] Y. Chaibi, M. Malvoni, A. Chouder, M. Boussetta, and M. Salhi. Simple and efficient approach to detect and diagnose electrical faults and partial shading in photovoltaic systems. *Energy Conversion and Management*, 196:330–343, 2019.
- [6] A. Singh Chaudhary and D. K. Chaturvedi. Analyzing defects of solar panels under natural atmospheric conditions with thermal image processing. *International Journal of Image, Graphics and Signal Processing*, 10(6):10–21, 2018.
- [7] J. Cohen. Nominal scale agreement with provision for scaled disagreement or partial credit. *Psychol. Bull.*, 70:213, Oct 1968.
- [8] C. Cortes and V. Vapnik. Support-vector networks. *Machine Learning*, 20(3):273–297, 1995.
- [9] T. Homem de Mello and G. Bayraktan. Monte carlo sampling-based methods for stochastic optimization. *Surveys in Operations Research and Management Science*, 19(1):56–85, 2014.

Table 3. Genetic fine-tuning results for the ten best individuals in the ResNet50+SVM and VGG16+SVM topologies, their characteristics, and metrics obtained using the DS2 dataset.

HCNN Topology	Lay.	N1	N2	Act.	Optim.	Drop.	κ	A_{cc}	R	S	P	$F-score$
VGG16+SVM	1	768	—	relu	adam	50%	0.7523	0.9534	0.9321	0.9538	0.9337	0.9441
VGG16+SVM	1	1024	768	tanh	sgd	40%	0.7235	0.9447	0.9243	0.9449	0.9214	0.9318
VGG16+SVM	1	512	—	selu	rmsprop	60%	0.7148	0.9312	0.9128	0.9325	0.9135	0.9246
VGG16+SVM	2	1024	—	relu	adam	30%	0.7452	0.9423	0.9249	0.9432	0.9256	0.9334
VGG16+SVM	1	768	—	elu	adadelta	50%	0.8017	0.9967	0.9712	0.9841	0.9742	0.9756
ResNet50+SVM	1	512	1024	exponential	adam	60%	0.7029	0.9328	0.9127	0.9215	0.9138	0.9241
ResNet50+SVM	2	512	512	tanh	rmsprop	50%	0.6941	0.9314	0.9146	0.9223	0.9131	0.9248
ResNet50+SVM	2	1024	—	relu	adam	40%	0.8526	0.9817	0.9645	0.9734	0.9623	0.9748
ResNet50+SVM	1	512	768	selu	sgd	30%	0.7324	0.9418	0.9234	0.9341	0.9216	0.9345
ResNet50+SVM	2	768	512	tanh	rmsprop	50%	0.7543	0.9523	0.9324	0.9431	0.9342	0.9436

Bold entries highlight the best-performing individuals in each topology.

Table 4. Examples of classifications performed by the VGG16+SVM model with data augmentation.

Imagem 1	Imagem 2	Imagem 3
		
Predito: Funcional Esperado: Funcional	Predito: Funcional Esperado: Funcional	Predito: Não funcional Esperado: Não funcional
Imagem 4	Imagem 5	Imagem 6
		
Predito: Não funcional Esperado: Não funcional	Predito: Não funcional Esperado: Não funcional	Predito: Funcional Esperado: Não funcional

- [10] S. Deitsch, C. Buerhop-Lutz, E. Sovetkin, A. Steland, A. Maier, F. Gallwitz, and C. Riess. Segmentation of photovoltaic module cells in uncalibrated electroluminescence images. *Machine Vision and Applications*, 32(4):84, May 2021.
- [11] S. Deitsch, V. Christlein, S. Berger, C. Buerhop-Lutz, A. Maier, F. Gallwitz, and C. Riess. Automatic classification of defective photovoltaic module cells in electroluminescence images. *Solar Energy*, 185:455–468, jun 2019.
- [12] M. Y. Demirci, N. Bešli, and A. Gümüüşçü. Efficient deep feature extraction and classification for identifying defective photovoltaic module cells in electroluminescence images. *Expert Systems with Applications*, 175:114810, 2021.
- [13] Deng, W. Dong, R. Socher, L.-J. Li, K. Li, and L. Fei-Fei. Imagenet: A large-scale hierarchical image database. In *2009 IEEE Conference on Computer Vision and Pattern Recognition*, pages 248–255, 2009.
- [14] A. E. Eiben and J. E. Smith. *Introduction to Evolutionary Computing*. Springer Publishing Company, 2 edition, 2015.
- [15] A. Et-taleby, Y. Chaibi, M. Boussetta, A. Allouhi, and M. Benslimane. A novel fault detection technique for pv systems based on the k-means algorithm, coded wireless orthogonal frequency division multiplexing and thermal image processing techniques. *Solar Energy*, 237:365–376, 2022.
- [16] T. Fan, S. Tao, X. Xiangying, L. Hu, and Z. Na. Automatic micro-crack detection of polycrystalline solar cells in industrial scene. *IEEE Access*, 10:16269–16282, 2022.
- [17] J. L. Fleiss. The equivalence of weighted kappa and the intraclass correlation coefficient as measures of reliability. *Educational and Psychological Measurement*, 33(3):613–619, 1973.
- [18] M. A. Islam, M. Hasanuzzaman, and N. A. Rahim. A comparative investigation on in-situ and laboratory standard test of the potential induced degradation of crystalline silicon photovoltaic modules. *Renewable Energy*, 127:102–113, 2018.
- [19] Z. A. Jaffery, A. K. Dubey, Irshad, and A. Haque. Scheme for predictive fault diagnosis in photo-voltaic modules using thermal imaging. *Infrared Physics & Technology*, 83:182–187, 2017.
- [20] U. Jahn, M. Herz, D. Parlevliet, M. Paggi, I. Tsanakas, J. Stein, K. Berger, S. Ranta, R. French, M. Richter, and et al. Review on infrared and electroluminescence imaging for pv field applications. techreport, International Energy Agency, Institute for Solar Energy Research Hamelin, Emmerthal (ISFH), Germany, March 2018. ISBN 978-3-906042-53-4.
- [21] G. Koch, R. Zemel, and R. Salakhutdinov. Siamese neural networks for one-shot image recognition. In *Proceedings of the 32nd International Conference on Machine Learning*, volume 37. Journal of Machine Learning Research, 2015.
- [22] R. Koha. A study of cross-validation and bootstrap for accuracy estimation and model selection. In *International Joint Conference on Artificial Intelligence IJCAI*, 1995.
- [23] S. R. Madeti and S.N. Singh. A comprehensive study on different types of faults and detection techniques for solar photovoltaic system. *Solar Energy*, 158:161–185, 2017.
- [24] S. R. Madeti and S.N. Singh. Monitoring system for photovoltaic plants: A review. *Renewable and Sustainable Energy Reviews*, 67:1180–1207, 2017.
- [25] M. L. McHugh. Interrater reliability: the kappa statistic. *Biochem. Med. (Zagreb)*, 22(3):276–282, 2012.
- [26] Z. Meng, S. Xu, L. Wang, Y. Gong, X. Zhang, and Y. Zhao. Defect object detection algorithm for electroluminescence image defects of photovoltaic modules based on deep learning. *Energy Science and Engineering*, 10(3):800–813, 2022.
- [27] K. A. K. Niazi, W. Akhtar, H. A. Khan, Y. Yang, and S. Athar. Hotspot diagnosis for solar photovoltaic modules using a naive bayes classifier. *Solar Energy*, 190(34-43), 2019.

Table 5. State-of-the-art results for defect detection in photovoltaic module cells compared with the best results of the proposed work.

Work	PV Cell	Algorithms	GFT	κ	A_{cc}	R	P	S	$F-Score$
[15]	Si-m and Si-p	CNN+SVM	✗	✗	0.9949 and 0.9946	✗	✗	✗	✗
[16]	Si-p	CNN	✗	✗	0.9911	0.9884	0.9697	✗	0.9790
[29]	Si-p	CNN	✗	✗	0.9300	✗	✗	✗	✗
[12]	Si-m and Si-p	k-NN, DT, RF, NB and L-CNN	✗	✗	0.9452	0.9736	0.9479	✗	0.9606
[1]	Si-m and Si-p	DS-CNN	✗	✗	✗	0.7375	0.7475	✗	0.7375
This work	Si-m and Si-p	HCNN	✓	0.8017	0.9967	0.9712	0.9841	0.9742	0.9756

✓ indicates the use of Genetic Fine-Tuning (GFT); ✗ indicates unavailable or unreported values.

- [28] G. Sombrio, P. L. Franzen, R. L. Maltez, L. G. Matos, M. B. Pereira, and H. Boudinov. Photoluminescence from sinxoy films deposited by reactive sputtering. *Journal of Physics D: Applied Physics*, 46(23):235106, May 2013.
- [29] W. Tang, Q. Yang, X. Hu, and W. Yan. Convolution neural network based polycrystalline silicon photovoltaic cell linear defect diagnosis using electroluminescence images. *Expert Systems with Applications*, 202:117087, 2022.
- [30] A. Tsanakas, L. Ha, and C. Buerhop. Faults and infrared thermographic diagnosis in operating c-si photovoltaic modules: A review of research and future challenges. *Renewable and Sustainable Energy Reviews*, 62:695–709, 2016.
- [31] S. van der Walt, J. L. Schönberger, J. Nunez-Iglesias, F. Boulogne, J. D. Warner, N. Yager, E. Gouillart, T. Yu, and scikit-image contributors. scikit-image: image processing in python. *PeerJ*, 2014.
- [32] P. Vieira, O. Sousa, D. Magalhães, R. Rabêlo, and R. Silva. Detecting pulmonary diseases using deep features in x-ray images. *Pattern Recognition*, 119:108081, 2021.
- [33] P. A. Vieira, D. M. V. Magalhães, A. O. Carvalho-Filho, R. M. S. Veras, R. A. L. Rabêlo, and R. R. V. Silva. Classification of covid-19 in x-ray images with genetic fine-tuning. *Computers and Electrical Engineering*, 96:107467, 2021.